Received: 21 July 2023 | Accepted: 19 November 2023

DOI: 10.1002/jpln.202300245

RESEARCH ARTICLE

Exploring the mechanisms of diverging mechanical and water stability in macro- and microaggregates

Svenja Roosch[1] | Vincent J. M. N. L. Felde[1] | Daniel Uteau[2] | Stephan Peth[1]

[1]Institute of Soil Science, Leibniz University Hannover, Hannover, Germany

[2]Department of Soil Science, University of Kassel, Witzenhausen, Germany

Correspondence
Svenja Roosch, Leibniz Universität Hannover, Institut für Bodenkunde, Herrenhäuser Straße 2, 30419 Hannover, Germany.
Email: roosch@ifbk.uni-hannover.de

This article has been edited by Ingrid Kögel-Knabner.

Funding information
Deutsche Forschungsgemeinschaft, Grant/Award Numbers: 276973637, 316923185

Abstract

Background: Soil stability is often evaluated using either mechanical or hydraulic stress. The few studies that use both approaches suggest that these two types of stability behave differently.

Aims: Our aim was to explore the mechanisms of aggregate stability regarding mechanical and water stability at the macro- and microscale, among other things, the effect of differing pore structure and soil organic matter content.

Methods: Samples were taken from two adjacent plots that were expected to differ in stability due to land use, that is, cropped versus bare fallow (BF). The stability of dry-separated macroaggregates (8–16 mm) and microaggregates (53–250 µm) was determined via wet sieving and unconfined uniaxial compression tests. To explore the mechanisms of stability, 3D pore characteristics were analyzed with microtomography scans. Furthermore, the contents of carbon and exchangeable polyvalent cations as well as contact angles were determined.

Results: Water stability of macroaggregates was much higher in the cropped plot (geometric mean diameter 0.65–2.37 mm [cropped] vs. 0.31–0.56 mm [BF]), while mechanical stability was very similar (median work 17.3 [cropped] and 17.5 N mm [BF]). The two size fractions behaved similarly regarding both types of stability, with more pronounced differences in macroaggregates. Several soil characteristics, like carbon, exchangeable calcium, and higher connectivity of pores to the aggregate exterior, contributed to water stability. Regarding mechanical stability, the destabilizing effect of lower carbon content and exchangeable calcium in the BF plot was counterbalanced by a lower porosity.

Conclusions: Mechanical and water stability behaved differently in the two plots due to the different deformation mechanisms.

KEYWORDS
bare fallow, computed tomography, mechanical stability, soil aggregates, water stability

1 | INTRODUCTION

1.1 | Soil stability—Definition, relevance, and measurement

Soil stability is understood as the ability of a soil to maintain its physical structure, that is, its spatial arrangement of solids and pores, against stresses. These stresses, and thus the corresponding stabilities, are usually divided into two types, mechanical and hydraulic. The stability of soils is of fundamental importance for many soil functions, especially in agriculture and forestry. As an example, the mechanical stability of a soil is related to its resistance against wind erosion or the maximal weight of a machine that it can bear without plastic deformation, while the hydraulic stability is related to its stability against water erosion due to heavy rainfall or flooding.

Methods used to study soil (aggregate) stability include dry and wet sieving procedures (Amézketa, 1999; Nimmo & Perkins, 2002) as well as confined and unconfined uniaxial compression tests (Dexter & Watts, 2000; Mosaddeghi et al., 2007). On the microaggregate scale, stability tests have mostly been limited to measurements of hydraulic stability, for example, by wet sieving (Al-Kaisi et al., 2014; Schweizer et al., 2019). To the best of our knowledge, methods for mechanical tests on single microaggregates have long been lacking. Recently, Felde et al. (2021) applied unconfined uniaxial crushing tests to microaggregates for the first time and found that mechanical stability tended to be higher in dry-separated microaggregates, compared to wet-sieved microaggregates from a Cambisol.

1.2 | Drivers and mechanisms of soil stability

If soil stability is defined by soil particles remaining in place despite forces acting upon them, anything that increases the strength of bonds between these particles will increase soil stability (Chenu & Cosentino, 2011). For example, polyvalent cations like calcium (Ca) act as cation bridges between negatively charged surfaces, such as clay particles or between clay and organic matter. Thus, they have a stabilizing effect on soil structure both regarding mechanical and water stability (Safar & Whalen, 2023; Wuddivira & Camps-Roach, 2007). Also, cementing and gluing substances like iron oxides and polysaccharides can stabilize particle contact points (Totsche et al., 2018). However, other aspects than the strength of individual particle–particle bonds can play a role, and these may differ between mechanical and hydraulic forces. Some main mechanisms are presented below.

Soil structure plays an important role in soil stability. When mechanical loads are applied to a given soil, the force is transmitted via the particle contact points. At a constant binding strength of contact points, an increasing number of particle contacts will increase the load that can be applied before deformation occurs (Hartge & Horn, 2016). Therefore, since a higher number of particle contacts requires higher packing density (when texture is constant), a lower porosity should correlate with higher mechanical stability. This has been confirmed in a modeling study (Wang & Arson, 2016). Particles with varying porosity were created by randomly deleting balls or groups of balls. Interestingly, tensile strength decreased quadratically with increasing total porosity, irrespective of the size of the individual cavities. However, this relation might not be as straightforward in real soils. For example, pore length rather than total porosity has been found to influence soil friability (Barbosa, Munkholm, et al., 2020).

Structural aspects can also influence water stability. For example, pore traits like pore size distribution and connectivity influence the velocity of water entry into the pore system and thus the build-up of air pressure, which causes slaking (Chenu & Cosentino, 2011).

Soil organic matter (SOM), respectively soil organic carbon (SOC), is generally assumed to stabilize soil structure (Abiven et al., 2009; Totsche et al., 2018). A range of mechanisms have been proposed, partly depending on the type of stability and the spatial scale (Chenu & Cosentino, 2011; Tisdall & Oades, 1982).

For example, enmeshment by fine roots and fungal hyphae is a mechanism that is considered relevant mainly at the macroaggregate scale. At smaller scales, SOM is assumed to glue primary particles together at their contact points as mentioned above. Finally, SOM, especially in the form of organic coatings, can increase soil hydrophobicity, which hinders or slows down water infiltration, thereby reducing slaking by compressed air (Chenu et al., 2000; Goebel et al., 2012). This can reduce initial aggregate destruction by slaking of aggregates that are immersed in water (Goebel et al., 2005, 2012). However, there is no consensus about the relevance of this latter mechanism (Dal Ferro et al., 2012; Zaher & Caron, 2008). In general, the stabilizing effect of SOM is complex, not always observed (Karlen et al., 1994; Roldán et al., 2003), and the mechanisms are not fully understood.

Clay can have diverging effects on soil stability. On the one hand, mechanical stability positively correlates with clay content (Kavdir et al., 2014). Scanning electron microscopy images of silt mixed with dispersed clay have shown the formation of wall-shaped bridges of clay between silt particles (Attou et al., 1998). On the other hand, differential swelling of clay upon wetting may contribute to aggregate destruction (Chenu & Cosentino, 2011). The latter effect also depends on the swelling behavior and thus on the mineralogy of the clay minerals (Reichert et al., 2009).

1.3 | This study

This study aimed to further our understanding of the mechanisms behind mechanical and hydraulic soil stability in cultivated Luvisol. It employed crushing tests both at macro- and microaggregate scales. These results were compared to wet sieving of both size fractions. Samples were taken from neighboring plots at the same site, so they were very similar in parent material, climate, relief, pedogenesis, and historic land use (arable). One of the two plots had been turned into continuous bare fallow (BF) 14 years before sampling. Due to the strongly reduced input of organic matter and the reduced tillage, we expected to measure differences in stability, which we aimed to explore with a set of subsequent measurements. A special focus was put on the differences

TABLE 1 Gravel contents of 8–16 mm aggregates as determined during wet sieving and texture of fine soil (<2 mm) of macroaggregates (8–16 mm) as determined by pipette method and wet sieving.

			Fine soil (<2 mm)		
Horizon	Sampling point	Gravel (%)	Clay (%)	Silt (%)	Sand (%)
Ap	Cropped R1	8.9	19.9	65.6	14.5
	Cropped R2	4.4	19.7	66.0	14.4
	Mean	6.7	19.8	65.8	14.5
	Bare fallow R1	4.1	19.4	65.1	15.6
	Bare fallow R2	4.2	20.5	65.2	14.3
	Mean	4.2	20	65.15	15
Bt	Cropped R1	3.7	20.5	66.7	12.8
	Cropped R2	2.7	20.3	66.8	12.9
	Mean	3.2	20.4	66.8	12.9
	Bare fallow R1	2.2	25.5	62.1	12.4
	Bare fallow R2	2.6	24.7	60.1	15.2
	Mean	2.4	25.1	61.1	13.8

Note: R1 and R2 refer to the replicate sampling points on each plot.

between mechanical and water stability while bearing in mind potential differences between macro- and microscales.

We hypothesized that:

1. Lower water stability can be explained with a higher wettability;
2. lower mechanical stability is related to a difference in soil structure, especially a higher porosity; and
3. differences in aggregate stability underlie the same behavior at the macro- and microaggregate scales.

2 | MATERIALS AND METHODS

2.1 | Field site and sampling

The site is located near Selhausen, Germany (50° 52'09.34'' N; 6° 27'00.58'' E; cf. also in the following: Meyer et al., 2017). The mean annual temperature is 10.2°C, and the mean annual precipitation is 714 mm (Bogena et al., 2018). The site is slightly inclined and rises ca. 4 m from west to east along a distance of 150 m (Meyer et al., 2017). The soil is a Luvisol derived from loess mixed with fluvial deposits. Consequently, the silt-dominated soil (42% to >70% silt in fine earth <2 mm) contains up to 60% (w/w) gravel in the top 30 cm with increasing gravel contents from west to east (Bornemann et al., 2011). Data on the texture at the positions sampled in this study are displayed in Table 1. Gravel contents were determined on 8–16 mm aggregates as part of the wet sieving procedure. Each value is the mean of three repeated measurements using ca. 20 g of aggregates each. The texture of fine soil (<2 mm) was determined on macroaggregates (8–16 mm) by pipette method and wet sieving. Each value is the mean of two repeated measurements (except "Bare fallow R2 Bt") using ca. 10 g of aggregates each.

A basic characterization of the soil at all sampling points was done including bulk density, pH, moisture, and inorganic C contents (Michaela Aehnelt, Tom Guhra, Kai U. Totsche; personal communication, 07/26/2022). The results are given in Table A1 in the Supporting Information.

In autumn 2005, an arable field at that site (ca. 1.1 ha) was turned to BF as part of a long-term experiment (Bogena et al., 2018). This was done by application of the herbicide glyphosate as soon as any vascular plants emerged (two to three times a year) and by shallow tillage (5-cm deep, once a year in 2006–2010, after 2010 every 4 years). The input of organic matter was thus drastically decreased. Consequently, SOC contents in the bulk topsoil (0–25 cm) of the BF plot decreased from 12 to 10 g kg^{-1} on average in 10 years (Meyer et al., 2017). This plot is called "BF" hereafter. The neighboring arable field (ca. 0.5 ha) was farmed with conventional tillage and is called "cropped" hereafter.

2.1.1 | Sampling

Sampling took place in November 2019. In the up-slope, the gravel content was too high to drive in soil cores. Therefore, samples were only taken in the middle of the slope (Figure A1 in the Supporting Information), where the soil had a high fine earth content (Schweizer et al., 2024). Samples were taken at two sampling points per plot and at two depths, at 5–11 cm (Ap horizon) and 35–41 cm (Bt horizon). At each sampling point and depth, five cores of minimally disturbed soil were extracted, resulting in 40 cores, each 6 cm in height and 10 cm in diameter. The five replicate soil cores were pooled after air-drying and removal from the core holders.

2.1.2 | Pretreatment of samples

In the lab, soil cores were air-dried for 48 h. Then they were removed from the core holder by gently hammering onto the metal. Any fragments that contained a visibly disturbed surface were discarded. The remaining fragments were dropped onto a sieve tower with mesh sizes 16, 8, and 2 mm. Large fragments were carefully broken by hand, so they would break along planes of weakness until they passed the 16-mm sieve. The resulting aggregate size fractions were stored dry and dark until analysis.

In order to isolate microaggregates from macroaggregates and avoid changes in texture associated with wet separation (Felde et al., 2021), we followed a dry separation procedure (ibid.): A subsample of the fraction <2 mm was crushed between two steel plates in a load frame at 250 µm min^{-1} until the steel plates were only 250-µm apart. The material was then sieved in a modified Casagrande apparatus (Mennerich Geotechnik) with 250, 53, and 20 µm mesh sizes, for 1000 taps at 2 Hz.

2.2 | Measurements

2.2.1 | Texture

Texture analysis was done using subsamples of the 8–16 mm aggregates. These were gently crushed (but not ground) in a mortar and sieved to <2 mm. Measurements were done in duplicates with wet sieving and sedimentation according to Köhn, including removal of SOM and iron oxides (DIN-ISO 11277, 2002). Deviating from ISO 11277, silt and clay were determined with the pipette method before sand fractions were wet-sieved. All fractions were dried at 105°C (sand for >15 h, silt and clay for >19 h) before weighing.

2.2.2 | Total carbon

Total C contents of macroaggregates were measured in duplicates (Vario ISOTOPE cube, Elementar Analysensysteme GmbH). Samples were milled in a ball mill prior to measurement. Total C contents of microaggregates were measured at Justus Liebig University Giessen (UNICUBE, Elementar Analysensysteme GmbH). This device could deal with the small sample amounts of 5–35 mg. These measurements could not be replicated due to the limited sample amount that was available.

2.2.3 | Polyvalent exchangeable cations

For measurement of polyvalent exchangeable cations, macroaggregates (8–16 mm) were crushed with pestle and mortar, suspended in 0.1 M $BaCl_2$ solution and shaken for 2 h. The filtered supernatant was analyzed in an inductively coupled plasma optical emission spectroscopy (ICP-OES) device (Agilent Technologies Ireland Ltd.) for contents of exchangeable Al, Ca, Fe, Mg, and Mn. Due to problems with the calibration for Al, it was excluded from further analysis.

2.2.4 | Mechanical stability

For the mechanical tests, uniaxial unconfined compression tests were done with single aggregates. In the following, these are referred to as crushing tests. The procedure was similar for micro- and macroaggregates, with the exceptions of start and end position, crushing speed, and piston size.

Macroaggregates from the 8 to 16 mm fraction were picked randomly (n = 50 per sample). If a large piece of gravel was visible, the aggregate was discarded; nevertheless, up to seven aggregates per sample had to be excluded afterward because the measurements were suspected to be disturbed by gravel (see Supporting Information for outlier selection). Each aggregate was placed onto a steel table mounted to a load frame (Zwick Roell Z100 AllroundLine, Zwick Roell). A metal piston 15 mm in diameter moved down at 2 mm min^{-1} until it was 3-mm away from the steel table. While moving down, a 100 N load cell recorded the force applied to the macroaggregate (Xforce HP 100 N, Zwick Roell; measurement error < ±1% from 0.2 N load). Simultaneously, the distance between the table and the piston was recorded digitally. The final separation of 3 mm was chosen to avoid the crushing of large mineral particles (gravel).

From the microaggregates (53–250 µm), specimens were chosen under a binocular, which were (1) among the largest in the fraction and (2) apparently no quartz grains (n = 100 per sample; for later outlier selection, see Supporting Information). The piston was 1 mm in diameter, and its movement speed was 250 µm min^{-1} until a separation at the end of the experiment of 25 µm, which was chosen to avoid crushing of medium-sized to large silt. The force applied to the microaggregate was measured by a load cell with 10 N capacity (Xforce HP 10 N, Zwick Roell; measurement error < ±1% from 0.02 N load).

2.2.5 | Water stability

Wet sieving measurements were done in duplicates. For macroaggregates (8–16 mm), ca. 20 g of soil was weighed and placed onto the top sieve of a tower of sieves with mesh sizes 8, 4, 2, 1, 0.5, and 0.25 mm. An aliquot of ca. 10 g was weighed in for determination of residual water content. The sieve tower was slowly lowered into a ton filled with tap water until the screen of the top sieve just touched the water surface. The aggregates were allowed to saturate in this position for 30 min. Then, the tower was carefully lowered until the aggregates were completely submerged and would stay under water during sieving. Aggregates were sieved for 10 min by means of an excenter motor with 4 cm vertical amplitude and at 0.27 Hz (16 oscillations min^{-1}). After the submerged sieving, the content of each sieve was dried overnight at 105°C, and the oven-dry weight was determined. The gravimetric water content in % as derived from the dried aliquots was used to correct the start weight of aggregates. Additionally, the weight of gravel (>2 mm) remaining in the sieves after sieving was also subtracted from the start weight. From the weight of dry soil in the sieves after sieving, the geometric mean diameter (GMD) was calculated as follows (Kemper & Rosenau, 1986):

$$GMD = \exp\left(\frac{\sum_{i=1}^{n} \ln(x_i) \cdot w_i}{\sum_{i=1}^{n} w_i}\right), \quad (1)$$

where x_i is the mean of the upper and lower limits of the ith size fraction, w_i is the mass of soil in the ith size fraction, and n is the number of size fractions. GMD was preferred above the more frequently reported mean weight diameter because aggregate size has been found to approximately follow a log-normal distribution (Gardner, 1956).

Wet sieving of microaggregates was done at the University of Bonn. For each measurement, ca. 2.5 g of dry-separated air-dry microaggregates (53–250 µm) were weighed and allowed to saturate for 5 min on a glass fiber filter paper that just touched the water surface (deionized water). Then the sample was cautiously washed with a spray bottle onto the screen of a sieve with 53 µm mesh size. The sieve tower was

submerged, and aggregates were sieved for 10 min at 0.5 Hz and 3-cm vertical amplitude with the help of an excenter motor. With this device, the movement of the sieve was not only vertical (as for the macroaggregates) but rather ellipsoid. The sieve content was transferred into glass beakers. An aliquot of the aggregates was weighed in a porcelain bowl and dried along with the beakers for 13 h at 105°C.

To correct for primary particles >53 µm, they were extracted from the wet-sieved fractions, and their weight was subtracted from both the start weight and the weight of water-stable aggregates (WSA). For this, wet sieved fractions were brought into suspension with 20 mL deionized water per g soil and 1 mL $(NaPO_3)_n$ solution per g soil (35.7 g $[NaPO_3]_n$ and 7.94 g Na_2CO_3 L^{-1}). The suspension was shaken overhead at 0.43 Hz (26 rounds min^{-1}) for 3 h. Additionally, the suspensions were diluted to 12.5 mg soil per mL and subjected to ultrasound at an energy level of 60 J mL^{-1}. After ultrasonication, suspensions were manually wet-sieved using a 53-µm sieve and dried at 105°C for 21 h and weighed.

2.2.6 | Aggregate structure

For the analysis of aggregate structure, microaggregates and macroaggregates were scanned with high-resolution X-ray microtomography (µCT). µCT scans of microaggregates were carried out with a Zeiss Xradia 520 Versa (Carl Zeiss AG) at the University of Kassel. For each plot, sampling point and depth, seven microaggregates (53–250 µm) were scanned, resulting in $2 \times 2 \times 2 \times 7 = 56$ scans in total. Each microaggregate was placed in a plastic container. One scan included 1600 projections with an acquisition time of 3 s each at an energy of 80 keV. Additional optical magnification lenses with 20× or 40× magnification were used, depending on the aggregate size. The positions of the detector and magnification lens were adapted for each aggregate individually to optimize image resolution. Voxel edge length was 0.5–0.8 µm for microaggregates.

For macroaggregates, only topsoil samples were used. For each plot and sampling point, three macroaggregates (8–16 mm) were scanned, resulting in $2 \times 2 \times 3 = 12$ scans. µCT scans were conducted with a Zeiss Xradia 520 Versa (see above) at the University of Hannover. Per scan, 1932 projections were taken, with 80 keV energy, an exposure time of 1.4 s, and a voxel edge length of 10.52 µm.

Additionally, the bulk density of macroaggregates was determined using submerged weighing similar to Uteau et al. (2013). Ten aggregates per plot and depth were first weighed, then dipped into hot paraffin wax to fill the pores and after cooling off were dip-weighed in water for determination of their volume. Dividing weight by volume gave the aggregate bulk density. Based on these data, total porosity was estimated assuming a solid particle density of 2.65 g cm^{-3}.

2.2.7 | Wettability

Contact angles were measured on intact and disturbed air-dry macroaggregates (8–16 mm) of the Ap horizon, using the sessile drop method according to Bachmann et al. (2000). Deviating from Bachmann et al. (2000), droplets of 1 µL of deionized water were placed onto the surface, and videos were recorded with a microscope (OCA 15, DataPhysics; 30 frames per second). The first image with a sharp droplet contour was analyzed using an ellipsoidal fit to the drop shape, a linear baseline and tangents on both sides of the drop (SCA 20 ver. 4.1.15, DataPhysics; Bachmann et al., 2021). If there was no picture with a sharp contour but the droplet did not spread immediately either, a contact angle of 1° was assumed.

For intact aggregates, 20 aggregates per sampling point were randomly picked; two droplets per aggregate were measured and the contact angles averaged per aggregate. For disturbed aggregates, aggregates were ground with pestle and mortar. One sample holder was prepared per sample, and five droplets were placed onto it such that the wetted areas did not touch. The values of the five repeated measurements were averaged.

Samples of the four sampling points were kept separate for all measurements. However, for the presentation of the results, results from the two replicate sampling points of each plot were merged.

2.3 | Data and image analysis

2.3.1 | Stability measurements

During the crushing tests, force, tool separation, and the resulting work at each time step were recorded. Since aggregates from one size class can still differ considerably in size, some standardization was considered necessary. Standardization of the work was done by expressing the energy needed for crushing an aggregate in relation to a fixed strain level, with strain defined as the relative change in aggregate diameter. As a proxy of diameter, the height of an aggregate was determined as the tool separation at the first contact between the sample and piston. Aggregates that were only slightly larger than the endpoint selected for the crushing test experienced only small percentages of height reduction. Additionally, tests were stopped when the force reached the maximum capacity of the load cell, which also resulted in lower maximal strain. The maximal strain that all aggregates experienced, 19%, was chosen as the level for comparison. Note that this is different from classical analyses of mechanical strength where the loading force at the point of aggregate failure (tensile strength) is determined (Rogowski, 1964). Such a definite aggregate failure, determined by a sudden force drop and visual appearance of a crack in the polar plane, does not seem to occur in most microaggregates.

Results from wet sieving of macroaggregates were expressed as GMD as described above. For wet sieving of microaggregates, only one sieve was used. Therefore, these results were expressed as a percentage of WSA.

2.3.2 | Image analysis

Image analysis of µCT scans of microaggregates included the following steps: A non-local means filter (Buades et al., 2011) was applied in

ImageJ/FIJI (Schindelin et al., 2012) for noise reduction. Segmentation was done with a global threshold as determined by Otsu's algorithm (Otsu, 1979). To prevent threshold determination from being disturbed by an over-representation of voxels representing air, segmentation was done in two iterations. The result of the first segmentation was dilated strongly to create a very rough mask of the aggregate. Then, the Otsu algorithm was applied again for threshold determination using only the voxels contained within the mask.

A spherical opening and closing (both $r = 1.5$ voxels) were applied to remove any objects smaller than 3 voxels in diameter. In order to separate aggregate solids from the plastic container and the pore space from the surrounding air, a more precise mask of the aggregate was created. For more details, please refer to the Supporting Information. The mask was applied both to the solid phase and to the inverted image with pores as foreground objects.

Quantitative analysis focused on the pore phase. The total pore volume divided by the volume of the aggregate mask gave the porosity. The pore size distribution was analyzed with the maximal inscribed ball method (Delerue et al., 1999). Each voxel was attributed the diameter of a maximal sphere that fit into the pore space and contained the voxel.

As a measure of connectivity, the Euler–Poincaré characteristic—also called Euler characteristic or Euler number—of the pore space with respect to the 26-neighborhood was calculated. For 3D objects, the Euler characteristic χ is defined as

$$\chi = N - C + H, \tag{2}$$

where N is the number of unconnected pores, C is the number of redundant connections, and H is the number of hollows (Vogel, 1997). It is worth noting that lower numbers are related to higher connectivity and that both positive and negative numbers are possible. Euler characteristic is expressed here as Euler density, that is, divided by aggregate volume.

For further characterization of the pore space structure, the pore space model was skeletonized in ImageJ/FIJI (algorithm by Lee et al., 1994), implemented by Ignacio Arganda-Carreras, version 2.1.1, 2017). The resulting skeletons were analyzed with the AnalyzeSkeleton function (Ignacio Arganda-Carreras, version 3.1.3, 2017). The largest skeleton in most cases contained >95% of the total branch length, which was calculated as the number of branches times of mean branch length. Therefore, only the results of the largest skeleton were selected for further analysis. The output was used to calculate median branch tortuosity, which is the ratio of the actual length of a branch and the Euclidean distance between its start and end points. Since shorter branches tend to be straighter (a branch that consists of only 2 voxels always has a tortuosity of 1), the median tortuosity of all branches was only calculated for branches that were longer than 10 voxels.

If not mentioned otherwise, image analysis was done with the proprietary software TooIIP by the Fraunhofer Institute for Industrial Mathematics (version 2019, Fraunhofer ITWM 2019) that comprises also functions from the MAVI kit (i.e., Modular Algorithms for Volume Images, same developer). All calculations were done in pixels or voxels and results were converted to µm or µm^3 in the end by multiplying with the (cubic) voxel edge length.

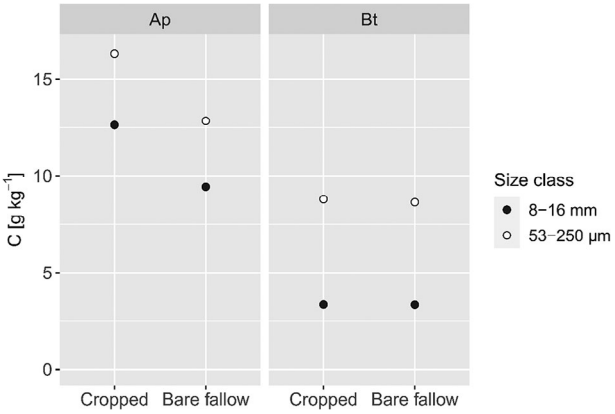

FIGURE 1 Total carbon contents of macro- and large microaggregates in g kg^{-1}. Each dot represents the mean of two sampling points and two repeated measurements each.

Analysis of macroaggregate µCT scans was similar to the procedure described above. However, scans had to be converted from 16- to 8-bit color depth first to reduce the size of the dataset. Histograms were cut off at manually chosen thresholds to ensure that the two peaks attributed to air-filled space and mineral particles were roughly at the same gray values for all scans. Other differences mainly concern adaptations to the different scales. For details, please refer to the Supporting Information. Since the macroaggregate scans just served as a supplementary measurement to test explanations for the results of water stability of macroaggregates, pore system analysis was restricted to total porosity, Euler density, and volume of pores connected to the outside. In contrast to microaggregate µCT scans, connectivity analysis for macroaggregates included all pores since the one largest pore of an aggregate was not as representative of its whole pore system as it was the case for microaggregates.

2.3.3 | Statement on replication and statistics

Because of their spatial proximity, neither replicate sampling points of one plot nor replicate aggregates of one sampling point were considered strictly statistically independent. Therefore, statistical tests were avoided to not give a false impression of certainty. Descriptive statistics were done with R (R Core Team, 2018).

3 | RESULTS

3.1 | Carbon contents

Generally, total C contents in both macro- and microaggregates were higher in the Ap than in the Bt horizon as expected (Figure 1). Compared to the cropped plot, aggregates from the BF plot had lower C contents in both aggregate size classes in the Ap. Notably, the absolute

TABLE 2 Polyvalent exchangeable cations in macroaggregates (8–16 mm).

Horizon	Sampling point	Ca $cmol_c\ kg^{-1}$	Fe	Mg	Mn	sum
Ap	Cropped R1	10.03	0.01	0.72	0.08	10.85
	Cropped R2	9.46	0.01	0.76	0.13	10.36
	mean	9.75	0.01	0.74	0.11	10.61
	Bare fallow R1	8.03	0.01	0.74	0.23	9.00
	Bare fallow R2	8.54	0.02	0.77	0.25	9.58
	mean	8.29	0.02	0.76	0.24	9.29
Bt	Cropped R1	6.88	0.01	0.53	0.08	7.49
	Cropped R2	6.82	0.02	0.53	0.07	7.45
	mean	6.85	0.02	0.53	0.08	7.47
	Bare fallow R1	8.67	0.02	1.01	0.11	9.81
	Bare fallow R2	9.64	0.01	1.08	0.05	10.77
	mean	9.16	0.02	1.05	0.08	10.29

difference between cropped and BF in the Ap horizon was the same, irrespective of size class and despite different absolute C contents (8–16 mm: $C_{cropped}-C_{BF}$ = 3.2 g kg^{-1}; 53–250 µm: $C_{cropped}-C_{BF}$ = 3.5 g kg^{-1}). Total C contents roughly equal organic C contents because previous analyses of the plot had revealed low inorganic C contents of 0.57 to 1.15 g kg^{-1} soil (Table A1).

3.2 | Polyvalent exchangeable cations

Polyvalent exchangeable cations at field pH were dominated by exchangeable Ca (6.85–9.75 $cmol_c\ kg^{-1}$; Table 2). Exchangeable Mg made some minor contributions in the range of 0.53 to 1.05 $cmol_c\ kg^{-1}$, while contents of exchangeable Fe and Mn were neglectable. The sum of polyvalent exchangeable ions tended to be higher in the cropped plot than in the BF plot (10.61 [cropped] vs. 9.29 $cmol_c\ kg^{-1}$ [BF]) in the Ap horizon. In the Bt horizon, the trend was opposite (7.47 [cropped] vs. 10.29 $cmol_c\ kg^{-1}$ [BF].

3.3 | Aggregate stability: Water stability

Wet sieving of dry-separated macroaggregates resulted in a clear difference between plots in the Ap horizon (Figure 2a). While in the cropped plot, GMD ranged from 0.65 to 2.37 mm and were thus highly variable, values in the BF plot were both lower and more uniform (0.31–0.56 mm). In the Bt horizon, the GMD was generally low and had very low variability (0.24–0.34 mm), irrespective of the plot. Thus, in the BF plot, macroaggregates from the Ap horizon were hardly more water-stable than aggregates from the Bt horizon.

The aggregate stability of dry-separated microaggregates against wet sieving was high with 75% to 85% WSA (Figure 2b). It has to be noted that sieving was impaired by a flat air bubble that remained under the mesh and prevented water from flowing through an estimated 20% of the mesh area. However, due to the ellipsoid movement of the sieve in the water, it seemed likely enough that particles smaller than the mesh opening size would eventually go through the screen.

There was a trend of aggregates from the BF plot to be less stable than the ones from the cropped plot. Notably, this was true for both horizons. In contrast to the macroaggregates, the water stability of microaggregates was only slightly lower in the Bt horizon (75.0%–83.5% WSA) than in the Ap horizon (80.2%–85.0% WSA).

3.4 | Aggregate stability: Mechanical stability

Water stability of macroaggregates was clearly different between plots in the Ap horizon and not different in the Bt horizon. In contrast, their mechanical stability behaved the opposite way (Figure 3a): In the Ap horizon, the mechanical work at 19% strain was not different between the plots (medians were 17.3 and 17.5 N mm in the cropped and BF plots, respectively). However, in the Bt horizon, the median work needed for that was higher in the BF than in the cropped plot (28.1 and 49.8 N mm in the cropped and BF plots, respectively). However, since the boxplots overlap almost completely, this difference should be considered only a trend. Additionally, the mechanical stability of macroaggregates was higher and more variable in the Bt horizon, compared to the Ap horizon.

Mechanical stability of microaggregates was not different between plots or horizons, neither in absolute level nor in variability (Figure 3b). The only exception from that was a slightly higher stability of microaggregates from the BF plot in the Bt horizon, compared to the cropped plot. The median work in the Ap horizon for 19% strain was 6.4×10^{-4} N mm (cropped) and 7.2×10^{-4} N mm (BF). In the Bt horizon, median work was 7.6×10^{-4} N mm (cropped) and 9.4×10^{-4} N mm (BF).

3.5 | Soil structure: Porosity, bulk density, connectivity, and tortuosity

In macroaggregates from the Ap horizon, resolvable pores had diameters in the range of 42 to 773 µm (Table 3). Resolved porosity was lower in the BF (4.2% ± 0.6%) than in the cropped plot (8.1% ± 1.6%). However, variability was high in the cropped plot (SE ± 1.6%). The pore size distribution showed that the porosity was dominated by the smallest resolved pores, here 42–100 µm in diameter (Figure A2 in the Supporting Information). In this pore size class, the largest difference between plots was observed, but also in the larger pore size classes, there was a trend toward lower volume fractions for the BF plot.

The image resolution only allowed us to analyze (part of) the macroporosity (>10 µm diameter). For comparison, the estimated total porosity based on the bulk density of macroaggregates was much higher with 39.0% ± 0.01% for the cropped plot and 34.8% ± 0.01% for the BF plot (Ap horizon; Table 3). The absolute difference roughly equals the absolute difference derived from µCT scans. Thus, although only a small part of total porosity was resolved in the µCT scans, the

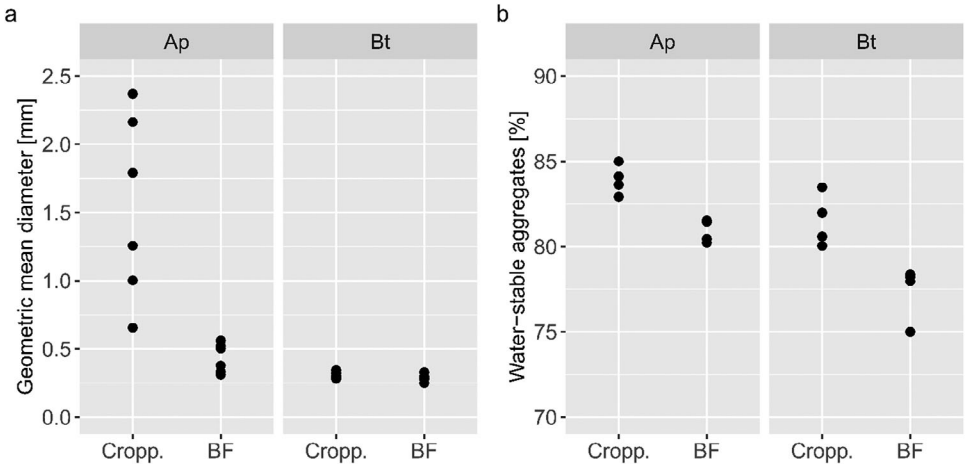

FIGURE 2 Results of wet sieving of macroaggregates (a) and microaggregates (b). For macroaggregates, $n = 6$ in each sample, resulting from three repeated measurements of the two replicate sampling points per plot. For microaggregates, $n = 4$ in each sample, resulting from two repeated measurements of the two replicate sampling points per plot. Note that the scale only ranges from 70% to 90%.

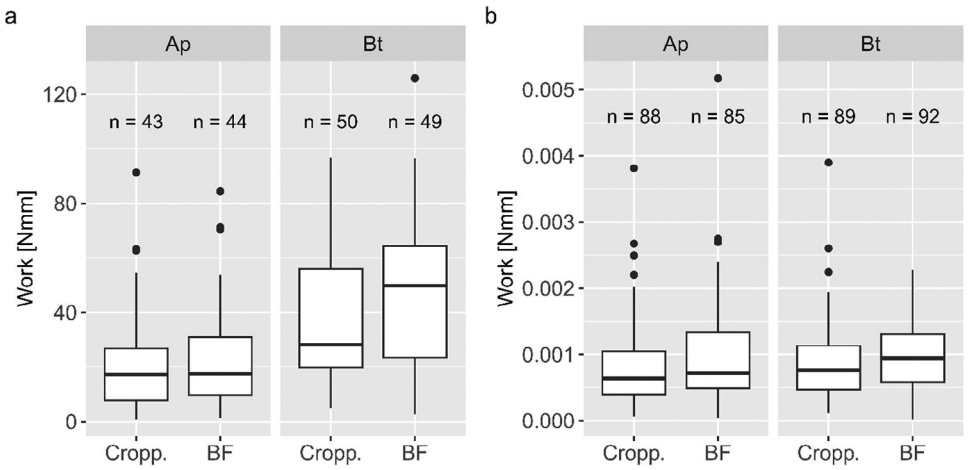

FIGURE 3 Results of individually crushed macroaggregates (a) and microaggregates (b), expressed as the work corresponding to 19% strain. Values of 14 and 35 of macro- and microaggregates, respectively, have been excluded as outliers (for details, see Supporting Information).

analyzed pore size range was where most of the difference between plots could be found.

The bulk density of macroaggregates (Table 3) also revealed a difference in the Bt horizon. Mean aggregate bulk density was slightly lower in the cropped plot (1.71 g cm^{-3}) than in the BF plot (1.75 g cm^{-3}).

For the microaggregates, µCT scans had a higher resolution, and thus diameters of resolved pores ranged from 2 µm to a maximum of 30 µm. In the Ap horizon, there was a trend of microaggregates from the BF plot to have a slightly lower resolved porosity (mean and SE: 25.2% ± 1.4%) than aggregates from the cropped plot (28.1% ± 0.8%). In the Bt horizon, this difference was even stronger (18.9% ± 1.1% [BF] vs. 25.2% ± 1.7% [cropped]). Similar to macroaggregate porosity, differences in porosity were largest in the smallest resolved pore size class with 2–5 µm diameter (Figure A3 in the Supporting Information).

The connectivity of resolved pores in microaggregates, expressed as Euler characteristic per 1000 $µm^3$ aggregate volume, almost mirrors the differences in porosity (Table 3). While in the Ap horizon, there was only a trend toward lower connectivity in the BF treatment (−1.27 [cropped] and −0.99 10^3 $µm^{-3}$ [BF]), there was a clearly lower connectivity in the BF plot in the Bt horizon (−0.27 10^3 $µm^{-3}$), compared to the cropped plot (−0.85 10^3 $µm^{-3}$). Note that lower values of Euler density mean higher connectivity. Numbers could only be negative because only the largest connected pore, that is, one object, was analyzed (see Section 2.3.2).

In macroaggregates, all pores were included in the analysis of connectivity. Consequently, Euler density was positive for all aggregates. The number of pores outweighed the number of redundant connections. In contrast to the microaggregate scale, Euler density was lower (and connectivity thus higher) in the BF treatment (50 mm^{-3}) than

TABLE 3 Pore characteristics as visible in microtomography scans with voxel edge lengths of 0.5–0.8 µm (microaggregates) and 10.5 µm (macroaggregates).

		Visible porosity (%)	Estimated total porosity (%)	Bulk density of macroaggregates (g cm^{-3})	Euler density (per aggregate volume) (1000 µm^{-3})	Tortuosity (–)	Volume of pores connected to outside per total aggregate volume (%)
Microaggregates (53–250 µm)							
Ap	Cropped	28.1 (0.8)	n.d.	n.d.	−1.27 (0.05)	1.24 (0.001)	n.d.
	Bare fallow	25.2 (1.4)	n.d.	n.d.	−0.99 (0.09)	1.24 (0.002)	n.d.
Bt	Cropped	25.2 (1.7)	n.d.	n.d.	−0.85 (0.11)	1.24 (0.003)	n.d.
	Bare fallow	18.9 (1.1)	n.d.	n.d.	−0.27 (0.08)	1.25 (0.002)	n.d.
Macroaggregates (8–16 mm)					**(mm^{-3})**		
Ap	Cropped	8.1 (1.6)	39.0 (0.01)	1.63 (0.02)	69 (1.8)	1.29 (0.007)	7.3 (1.6)
	Bare fallow	4.2 (0.6)	34.8 (0.01)	1.75 (0.02)	50 (5.7)	1.27 (0.004)	3.4 (0.6)
Bt	Cropped	n.d.	36.2 (<0.01)	1.71 (0.01)	n.d.	n.d.	n.d.
	Bare fallow	n.d.	34.0 (<0.01)	1.75 (0.01)	n.d.	n.d.	n.d.

Note: Mean values with standard error in parentheses. $n = 14$ for microaggregates (except Bt, cropped with $n = 12$ and Bt, bare fallow with $n = 13$) and $n = 3$ for macroaggregates. Estimated total porosity based on bulk density measurements of macroaggregates with $n = 20$. n.d. means "not determined."

in the cropped plot (69 mm^{-3}). However, the volume of pores connected to the air space around the aggregates tended to be higher in the cropped plot (7.3%) than in the BF plot (3.4%; data not shown). The share of total resolvable porosity that was connective to the air space outside the aggregate was high (>75% of total visible porosity in all but one case) and slightly higher in the cropped plot than under BF (Figure A4 in the Supporting Information).

The mean pore tortuosity in microaggregates showed no evidence of a difference between plots or horizons. In the Ap horizon, the mean tortuosity was 1.24 in both plots. In the Bt horizon, tortuosities were similar with mean values of 1.24 (cropped) and 1.25 (BF). The tortuosity of macropores in macroaggregates from the Ap horizon was slightly higher in the cropped (mean and SE 1.29 ± 0.007) than in the BF plot (1.27 ± 0.004).

3.6 | Contact angles of crushed and intact macroaggregates

Contact angle measurements were methodologically challenging. On the intact aggregates, it was hard to find a more or less flat surface to place the droplet on. On the plates with the crushed material attached, the droplets often spread so quickly that the camera did not capture a sharp picture of the initial droplet. Considering this uncertainty, the results have to be interpreted with caution. Thus, despite a slightly higher median contact angle of intact macroaggregates in the BF (9.0°), compared to the cropped plot (4.3°), no difference between the plots could be found (Figure 4). Also in the crushed aggregates, no clear difference was observed. The gap in values between 1° and 7.25° hints at an insufficient frame rate (30 frames per second) for a highly wettable soil.

4 | DISCUSSIONS

4.1 | Water stability versus mechanical stability

Water stability and mechanical stability of aggregates from the Ap horizon showed opposite trends between the two plots. The stability of aggregates against water was generally reduced under BF as already described by Tisdall and Oades (1982) and observed for the same site (Siebers et al., 2023). The effect was much weaker in microaggregates. In contrast, mechanical stability was similar or even slightly increased in the BF plot in both macro- and microaggregates. Diverging behavior was also observed in the Bt horizon. While water stability was not different (macroaggregates) or only slightly lower in the BF plot (microaggregates), mechanical stability was higher in the BF plot (macroaggregates) or similar between plots (microaggregates). Note that since aggregates had similar gravimetric water contents, we do not expect water content to have disturbed comparability of stability measurements (Figure A5 in the Supporting Information).

This diverging behavior between mechanical and water stability has been observed before. For example, Daraghmeh et al. (2009) found reduced mechanical stability but increased water stability under reduced tillage, compared to conventional tillage. However, the increasing effect on water stability was only present when water stability was measured on air-dried aggregates, not when they were field-moist. Similarly, Kogut et al. (2019), comparing a Chernozem under 52 years of tilled BF to the same soil under steppe, found a mixed effect on mechanical stability. In contrast, water stability was strongly decreased under BF. Of the air-dry 1–2 mm aggregates, 80% were stable against wet sieving under steppe, while under BF, only 0.3% were water-stable. This is in line with previous findings that water stability and mechanical stability are not well correlated (Jozefaciuk & Czachor,

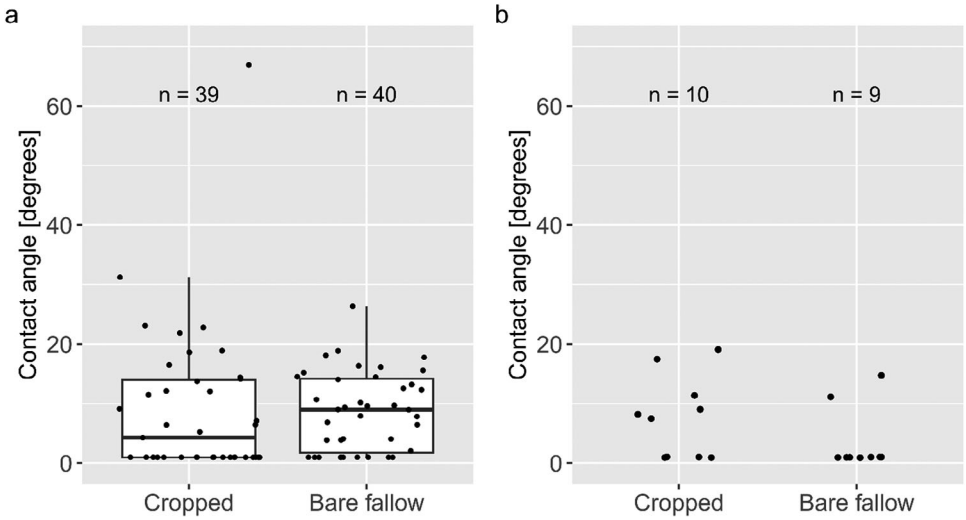

FIGURE 4 Contact angles of intact (a) and crushed (b) macroaggregates from the Ap horizon. For intact aggregates, each dot refers to one aggregate and is the mean of two droplets per aggregate. For crushed aggregates, each dot refers to one droplet. One plate was prepared per sampling point and five droplets were placed on each plate.

2014). This lack of correlation implies that the two types of stability rely on different mechanisms, which are discussed in the following subsections.

4.2 | Mechanisms of water stability

The hypothesized explanation for the lower water stability of macroaggregates under BF was that loss of SOM increased the wettability of the soil and thus enhanced the disrupting effect of slaking (Chenu et al., 2000). However, contact angles were not different between BF and cropped in our study, neither on intact nor on homogenized aggregates. All samples were highly wettable. Given the high specific surface area of silty soil, the amount of organic matter present in the soil was not sufficient to hydrophobize the particles to a measurable degree.

Other factors influencing the velocity of water entry include characteristics of the pore system. The median tortuosity of pore branches was not different between samples. In contrast, the pore size distribution of macroaggregates was different between plots. Aggregates from the BF plot had a lower porosity in all visible pore size classes, but the difference was strongest in the smallest visible pore sizes (42–100 µm; Figure A2 in the Supporting Information). Since smaller pores have a higher matric potential, a reduction in small pores, *ceteris paribus*, reduces the velocity of water entry and is likely to lead to a weaker slaking effect—the opposite of what was observed. However, a large range of pore sizes—any pores <42 µm in diameter—could not be resolved in the µCT scans.

Pore system characteristics are not only relevant for the entry of water but also for the escape of air. A highly connective pore system enables the air to escape more easily, alleviating the build-up of air pressure (Chenu & Cosentino, 2011). Surprisingly, connectivity as indicated by Euler density was lower in the cropped plot. However, one has to take into account that below the resolution limit, some apparently unconnected pores are in fact connected. Consequently, a higher porosity is likely to go along with a higher number of apparently unconnected pores. It is therefore expected that the higher porosity of macroaggregates from the cropped plot coincides with a lower resolvable connectivity.

This implies that Euler density does not always reflect the aspects of connectivity that affect the escape of air upon wetting. One of these aspects is the connectivity of pores to the soil (here: aggregate) surface. We therefore calculated the percentage of pore volume that was connected to the air outside macroaggregates and found this percentage to be slightly lower under BF (Figure A4 in the Supporting Information). We conclude that regarding the pore structure, macropore connectivity to the aggregate surface rather than overall macropore Euler density influenced resistance against slaking in macroaggregates.

Differences in organic carbon contents can also affect aggregate stability through enmeshment and gluing (Totsche et al., 2018). However, the fine structures of hyphae and fine roots are likely to become brittle when dried. The air-drying before wet sieving is likely to have strongly weakened the enmeshment effect if there was any. Therefore, physicochemical interactions seem to be the most likely mechanism for how lower SOM content reduced the water stability of macroaggregates in the BF plot. However, in a lab incubation experiment inducing SOM depletion on soil cores from a carbonate-free agricultural site (Luvisol), water stability did not change significantly over time (300 days; Bucka et al., 2023). The authors concluded that the sites of initial SOM loss did not contribute to gluing particles together. SOC contents and losses in that experiment were similar to the field experiment presented here: Of the initial 11.2 g C kg^{-1} soil, 2.2 g C kg^{-1} were lost via respiration and leaching. The main difference to field conditions was the constant water tension and temperature, which excluded the stresses exerted by wetting/drying and freezing/thawing, and limited leaching intensity. In our study, particle–particle contacts and also organo-mineral associations may have additionally been weakened by

a lower content of exchangeable Ca in the BF plot (8.29 $cmol_c\ kg^{-1}$) than in the cropped plot (9.75 $cmol_c\ kg^{-1}$; Table 2). Summing up, the observed lower water stability of macroaggregates in the BF plot is attributed to a combination of lower contents of SOM and exchangeable Ca and a difference in pore structure with less pores connected to the aggregate exterior.

Concerning the slightly reduced water stability of microaggregates under BF, increased wettability can be ruled out for the reasons described above. Enmeshment by roots and fungal hyphae can be dismissed also because it is not relevant at this scale (Tisdall & Oades, 1982). Thus, differences in the pore system and in gluing by organic matter, for example, extracellular polymeric substances, remain as explanations as was the case at the macroaggregate scale. Additionally, differences in cementing substances like oxides can play a major role at this scale (Lipiec et al., 2018; Totsche et al., 2018), which has been studied for the same site (Siebers et al., 2023).

Similar to the macroaggregates, microaggregates under BF had lower resolvable porosity (>2 μm; for pore size distribution, see Figure A3 in the Supporting Information). In contrast to macroaggregates, this lower porosity went along with a lower connectivity of the largest connected pore network. This could be an indicator of aggregates being more susceptible to slaking. Despite this supposed vulnerability, microaggregates under BF were only slightly less water-stable than microaggregates from the cropped plot. From this, one can conclude that disruption by entrapped air does not play a large role at this scale and/or that gluing or cementing substances stabilized particle contact points.

In the cropped plot, where clay contents were similar in both horizons (ca. 20%), microaggregates from the Bt horizon were only slightly less stable than aggregates from the Ap horizon. However, in the Bt horizon of the BF plot, where clay content was ca. 25%, water stability was clearly reduced, compared to the Ap horizon (ca. 20% clay). We suspect differential swelling of clay as the cause (Chenu & Cosentino, 2011).

4.3 | Mechanisms of mechanical stability

Mechanical stability was not lower in the BF plot and hence apparently not affected by the decline in C contents that occurred in both macro- and microaggregates. Nevertheless, differences in structure have been measured. As mentioned above, the BF plot had a lower macroporosity, which is in line with a higher bulk density of macroaggregates (Table 3) and of the bulk soil (Table A1 in the Supporting Information). Similarly, porosity in the range of 2−10 μm was reduced in microaggregates. These changes can only come through the rearrangement of particles, which requires particles to be detached from their original neighboring particles (and new particle contact points being created). If the forces in the field are the same but rearrangement of particles happens in the one plot but not in the other, it is reasonable to assume that the connections between particles were weaker.

Alternatively, it is possible that particle connections in both plots have the same strength, and higher porosity in the cropped plot is simply induced by the regular disturbance through tillage, leaving not enough time in between for the soil to settle completely (Chen et al., 2016). However, this is not realistic for the pore sizes included in microaggregates since these structures are generally considered to be too stable to be affected by mechanical impact during tillage (Six et al., 2000; Tisdall & Oades, 1982). Thus, the reduced porosity hints toward an initial destabilization of particle contacts followed by the rearrangement of particles.

The process of destabilization and the kinds of forces that may have detached particles are not clear. We speculate that the loss of SOM and exchangeable Ca destabilized particle contacts and consequently forces exerted, for example, by freezing/thawing detached particles. These loosened particles partly filled pores, leading to a lower porosity and a higher average number of inter-particle contacts per particle. At a given strength of bonds between particles, this results in a mechanical stability (Barbosa, Keller, & de Oliveira Ferraz, 2020). Since mechanical stability was not increased, bond strength must have been reduced. So, two opposite mechanisms supposedly balanced out each other: The mechanical stability was initially decreased by a weakening of particle bond strength but increased again due to the higher number of particle contacts.

Another reason for the lack of a measurable difference in mechanical stability could lie in the crushing method. As described in Section 2, a minimal distance at the end of each crushing test was defined to avoid single large particles carrying the load exerted by the load frame. However, especially measurements of microaggregates often seemed to be affected by this as sometimes notable by a cracking sound while crushing or a sudden force drop after a steep linear increase in force. Sorting out outliers afterward was difficult since no objective criteria exist on how to safely distinguish a single mineral particle from connected particles by the force–displacement curve. We alleviated this effect by restricting the analysis to the initial phase of the crushing tests (first 19% strain). However, the variance of results within one sample might decrease if this effect could be further reduced.

Moreover, there might be criteria other than the work needed for a certain level of strain that are better indicators of mechanical strength. Notably, the frequent notion of "aggregate failure," for example, defined by the emergence of equatorial cracks as suggested by Barbosa and de Oliveira Ferraz (2020) is not suitable for microaggregates because these distinct equatorial cracks do not seem to occur at this scale. Furthermore, the shape of microaggregates can strongly deviate from a sphere, which violates a basic assumption of the concept of tensile strength measured by the force at aggregate rupture (Rogowski et al., 1968). A further adaptation of the method is thus necessary.

It has to be noted, though, that the method was capable of detecting a higher stability in the BF plot, compared to the cropped plot in the Bt horizon. This difference was much more pronounced in macro- than in microaggregates. As mentioned before, there was a difference in clay content (20% [cropped] vs. 25% [BF]), which affected mean aggregate bulk density (1.71 g cm^{-3} [cropped] vs. 1.75 g cm^{-3} [BF]). In the absence of a difference in SOM content, the effect of an increased number of particle contacts—and tightly held water between

the clay particles—in the BF plot manifests itself in a higher mechanical stability.

4.4 | Macro- versus microaggregates

As commonly observed, macroaggregates were more stable than microaggregates. In terms of the work needed for 19% height reduction, values for microaggregates compared to macroaggregates were smaller by 4 orders of magnitude while their volume and weight were smaller by 5 orders of magnitude (data not shown). In terms of water stability, most macroaggregates already disintegrated during saturation while the majority of microaggregates remained stable. Notably, the two aggregate size classes showed trends in the same direction (or no trend for both) in both mechanical and water stability regarding the differences between plots. It is remarkable that even microaggregates showed differences in structure and water stability since they are usually considered too small to be affected by agricultural management. This means that not even these small and rather stable structures may not provide permanent physical protection for SOM against decay. However, microaggregates usually are separated via wet sieving, while in our study, a dry sieving approach was used. Felde et al. (2021), who developed this separation method, observed that it preserved microaggregate structure better than wet separation. This method enables soil scientists to better study how microscale soil structures are affected by land use.

4.5 | Site-specific versus treatment-induced differences between plots

When considering differences between plots, we have to keep in mind that due to lack of replication, we cannot be sure whether these differences were caused by the differing land use or by previous spatial heterogeneity of the experimental site. For example, the difference between plots in exchangeable Ca (Ap horizon) may on the one hand have existed at the beginning of the experiment due to differential liming. On the other hand, BF can reduce pH (Curtin et al., 2015), for example, due to nitrification and production of carbonic acid from microbial respiration. H^+ partly replace Ca ions at the exchange sites, so the latter are more susceptible to leaching. BF was most likely also the cause of SOM loss and thus loss of cation exchange sites, which also increases the risk of Ca leaching. Due to this uncertainty of attribution, we focused on the soil parameters that can explain differences in soil stability. Whether these parameters were different due to land use can to some degree be argued but cannot be tested based on our data.

5 | CONCLUSION

The stability of dry-separated aggregates differed between BF and the cropped plot but mechanical and water stability diverged: Water stability differed most between plots in the Ap horizon and was lower in the BF plot, while mechanical stability was similar. In contrast, water stability was similar in both plots in the Bt horizon, whereas mechanical stability was higher in the BF plot. We confirmed that macro- and microaggregates showed trends in the same direction, but stability was higher and differences between plots were generally smaller in microaggregates. Nevertheless, it is notable that also microaggregates showed differences in stability between plots. This is in contrast with the general perception that microaggregates are too small and stable to be affected by agricultural management and deserve attention in future research.

In contrast to our hypothesis, the difference in water stability of topsoil aggregates was not determined by wettability because contact angles were the same in both plots. This corroborates the doubts that have been raised about the relative importance of wettability to slaking, at least for silty soils with a generally low SOM content. Instead, we attribute the lower water stability under BF to weaker particle contacts due to lower contents of SOM and exchangeable Ca and to higher air pressure during wetting due to a lower connectivity of macropores to the aggregate surface.

Mechanical stability was not different between plots in the Ap horizon despite a difference in soil structure, especially porosity. We assume that weaker particle contacts due to lower SOM and Ca contents transiently made the soil susceptible to mechanical impacts of, for example, freezing and thawing. The resulting denser packing increased the number of particle contact points, compensating for their reduced individual strength. The higher mechanical stability of aggregates from the Bt horizon under BF was attributed to a higher clay content while it had the opposite effect on water stability (microaggregates). Due to this ambivalent effect of clay on mechanical and water stability, these two types of stability can be expected to differ strongly in soils that contain high amounts of expansive clay. Further research should compare the relation of mechanical and water stability and their mechanisms across different soil types. This could help reveal trade-offs and synergies between soil characteristics regarding the different types of soil stability and help design land management practices that keep both in an optimal range.

We critically reflected on the crushing method used to determine aggregate stability, especially when applied at the microaggregate scale and encourage a further development of uniaxial unconfined compression tests and derived parameters to measure mechanical stability at a wide range of scales.

ACKNOWLEDGMENTS

This study was conducted within the research unit "*MADSoil—Microaggregate Development in Soil: Formation and turnover of the structural building blocks of soils*," which is funded by the *DFG (Deutsche Forschungsgemeinschaft) (DFG RU 2179*, project no. *276973637*). µCT scans of macroaggregates have been conducted with an X-ray microscope that was financed by the *DFG* (project no. *316923185*) at Leibniz University Hannover, Institute of Materials Science, by *Christoph Kahra*. Open access publication financed via project *DEAL* . We thank *Dymphie Burger* and *Wulf Amelung* (University of Bonn) for their help with the wet sieving of microaggregates and *Elke Müller* (University of Giessen) for

conducting the element analysis of microaggregates. Three anonymous reviewers greatly helped to improve the manuscript.

Open access funding enabled and organized by Projekt DEAL.

DATA AVAILABILITY STATEMENT

The data that support the findings of this study are available from the corresponding author upon reasonable request.

ORCID

Svenja Roosch https://orcid.org/0000-0002-6807-2487
Vincent J. M. N. L. Felde https://orcid.org/0000-0002-1018-2376
Daniel Uteau https://orcid.org/0000-0003-1499-4344
Stephan Peth https://orcid.org/0000-0001-9799-212X

REFERENCES

Abiven, S., Menasseri, S., & Chenu, C. (2009). The effects of organic inputs over time on soil aggregate stability—A literature analysis. *Soil Biology and Biochemistry*, *41*(1), 1–12.

Al-Kaisi, M. M., Douelle, A., & Kwaw-Mensah, D. (2014). Soil microaggregate and macroaggregate decay over time and soil carbon change as influenced by different tillage systems. *Journal of Soil and Water Conservation*, *69*(6), 574–580.

Amézketa, E. (1999). Soil aggregate stability: A review. *Journal of Sustainable Agriculture*, *14*(2-3), 83–151.

Attou, F., Bruand, A., & Le Bissonnais, Y. (1998). Effect of clay content and silt—Clay fabric on stability of artificial aggregates. *European Journal of Soil Science*, *49*(4), 569–577.

Bachmann, J., Horton, R., Van Der Ploeg, R. R., & Woche, S. (2000). Modified sessile drop method for assessing initial soil–water contact angle of sandy soil. *Soil Science Society of America Journal*, *64*(2), 564–567.

Bachmann, J., Söffker, S., Sepehrnia, N., Goebel, M. O., & Woche, S. K. (2021). The effect of temperature and wetting–drying cycles on soil wettability: Dynamic molecular restructuring processes at the solid–water–air interface. *European Journal of Soil Science*, *72*(5), 2180–2198.

Barbosa, L. A. P., Munkholm, L. J., Obour, P. B., & Keller, T. (2020). Impact of compaction and post-compaction vegetation management on aggregate properties, Weibull modulus, and interactions with intra-aggregate pore structure. *Geoderma*, *374*, 114430. https://doi.org/10.1016/j.geoderma.2020.114430

Barbosa, L. A. P., & de Oliveira Ferraz, A. C. (2020). Which evidence attests for soil aggregate rupture? A new criterion to determine aggregate tensile strength. *Soil and Tillage Research*, *197*, 104530. https://doi.org/10.1016/j.still.2019.104530

Barbosa, L. A. P., Keller, T., & de Oliveira Ferraz, A. C. (2020). Scale effect of aggregate rupture: Using the relationship between friability and fractal dimension to parameterise discrete element models. *Powder Technology*, *375*, 327–336.

Bogena, H. R., Montzka, C., Huisman, J. A., Graf, A., Schmidt, M., Stockinger, M., von Hebel, C., Hendricks-Franssen, H. J., van der Kruk, J., Tappe, W., Lücke, A., Baatz, R., Bol, R., Groh, J., Pütz, T., Jakobi, J., Kunkel, R., Sorg, J., & Vereecken, H. (2018). The TERENO-Rur Hydrological Observatory: A multiscale multi-compartment research platform for the advancement of hydrological science. *Vadose Zone Journal*, *17*(1), 1–22.

Bornemann, L., Herbst, M., Welp, G., Vereecken, H., & Amelung, W. (2011). Rock fragments control size and saturation of organic carbon pools in agricultural topsoil. *Soil Science Society of America Journal*, *75*(5), 1898–1907.

Buades, A., Coll, B., & Morel, J. M. (2011). Non-local means denoising. *Image Processing On Line*, *1*, 208–212. https://doi.org/10.5201/ipol.2011.bcm_nlm

Bucka, F. B., Felde, V. J., Peth, S., & Kögel-Knabner, I. (2023). *Detecting the disintegration: Insights into soil structure decay following OC depletion* (No. EGU23–6871). Copernicus Meetings. https://doi.org/10.5194/egusphere-egu23–6871

Chen, Q., Kravchenko, Y. S., Li, H., Chen, S., & Zhang, X. Y. (2016). Seasonal variation of physical and chemical properties in a black soil under No-till and conventional tillage in Northeast China. *Philippine Agric Scient*, *99*, 277–282.

Chenu, C., & Cosentino, D. (2011). Microbial regulation of soil structure dynamics. In K. Ritz & I. Young (Eds.), *The architecture and biology of soils—Life in inner space* (pp. 37–70). CAB International.

Chenu, C., Le Bissonnais, Y., & Arrouays, D. (2000). Organic matter influence on clay wettability and soil aggregate stability. *Soil Science Society of America Journal*, *64*(4), 1479–1486.

Curtin, D., Fraser, P. M., & Beare, M. H. (2015). Loss of soil organic matter following cultivation of long-term pasture: Effects on major exchangeable cations and cation exchange capacity. *Soil Research*, *53*(4), 377–385.

Dal Ferro, N., Berti, A., Francioso, O., Ferrari, E., Matthews, G. P., & Morari, F. (2012). Investigating the effects of wettability and pore size distribution on aggregate stability: The role of soil organic matter and the humic fraction. *European Journal of Soil Science*, *63*(2), 152–164.

Daraghmeh, O. A., Jensen, J. R., & Petersen, C. T. (2009). Soil structure stability under conventional and reduced tillage in a sandy loam. *Geoderma*, *150*(1-2), 64–71.

Delerue, J. F., Perrier, E., Yu, Z. Y., & Velde, B. (1999). New algorithms in 3D image analysis and their application to the measurement of a spatialized pore size distribution in soils. *Physics and Chemistry of the Earth, Part A: Solid Earth and Geodesy*, *24*(7), 639–644.

Dexter, A. R., & Watts, C. W. (2000). Tensile strength and friability. In K. A. Smith & C. E. Mullins (Eds.), *Soil and environmental analysis: Physical Methods* (2nd ed., pp. 405–433). Marcel Dekker, Inc.

DIN-ISO 11277. (2002). *Bodenbeschaffenheit: Bestimmung der Partikelgrößenverteilung in Mineralböden—Verfahren mittels Siebung und Sedimentation*. Deutsches Institut Für Normung, Beuth Verlag GmbH.

Fechner, A., Mikutta, R., Kaiser, K., Bromm, T., Vogel, C., Zethof, J., Aehnelt, M., Guggenberger, G., & Dultz, S., (2023). Changes in soil organic matter quality during long-term bare fallow do not affect microaggregate stability. *EGU General Assembly 2023*, Vienna, Austria, 24–28 Apr 2023, EGU23-15453. https://doi.org/10.5194/egusphere-egu23-15453, 2023.

Felde, V. J. M. N. L., Schweizer, S. A., Biesgen, D., Ulbrich, A., Uteau, D., Knief, C., Graf-Rosenfellner, M., Kögel-Knabner, I., & Peth, S. (2021). Wet sieving versus dry crushing: Soil microaggregates reveal different physical structure, bacterial diversity and organic matter composition in a clay gradient. *European Journal of Soil Science*, *72*(2), 810–828.

Gardner, W. R. (1956). Representation of soil aggregate-size distribution by a logarithmic-normal distribution. *Soil Science Society of America Journal*, *20*(2), 151–153.

Goebel, M. O., Bachmann, J., Woche, S. K., & Fischer, W. R. (2005). Soil wettability, aggregate stability, and the decomposition of soil organic matter. *Geoderma*, *128*(1-2), 80–93.

Goebel, M. O., Woche, S. K., & Bachmann, J. (2012). Quantitative analysis of liquid penetration kinetics and slaking of aggregates as related to solid–liquid interfacial properties. *Journal of Hydrology*, *442*, 63–74.

Hartge, K.-H., & Horn, R. (2016). *Essential soil physics—An introduction to soil processes, functions, structure and mechanics*. Schweizerbart'sche Verlagsbuchhandlung. http://www.schweizerbart.de//publications/detail/isbn/9783510652808/Einfuhrung_in_die_Bodenphysik

Jozefaciuk, G., & Czachor, H. (2014). Impact of organic matter, iron oxides, alumina, silica and drying on mechanical and water stability of artificial soil aggregates. Assessment of new method to study water stability. *Geoderma*, *221*, 1–10.

Karlen, D. L., Wollenhaupt, N. C., Erbach, D. C., Berry, E. C., Swan, J. B., Eash, N. S., & Jordahl, J. L. (1994). Crop residue effects on soil quality following 10-years of no-till corn. *Soil and Tillage Research*, *31*(2-3), 149–167.

Kavdir, Y., Zhang, W., Basso, B., & Smucker, A. J. (2014). Development of a new long-term drought resilient soil water retention technology. *Journal of Soil and Water Conservation*, *69*(5), 154A–160A.

Kemper, W. D., & Rosenau, R. C. (1986). Aggregate stability and size distribution. In A. Klute (Ed.), *Methods of soil analysis, Part 1. Physical and mineralogical methods* (pp. 425–442). ASA.

Kogut, B. M., Artemyeva, Z. S., Kirillova, N. P., Yashin, M. A., & Soshnikova, E. I. (2019). Organic matter of the air-dry and water-stable macroaggregates (2–1 mm) of Haplic Chernozem in contrasting variants of land use. *Eurasian Soil Science*, *52*, 141–149.

Lee, T. C., Kashyap, R. L., & Chu, C. N. (1994). Building skeleton models via 3-D medial surface axis thinning algorithms. *CVGIP: Graphical Models and Image Processing*, *56*(6), 462–478.

Lipiec, J., Świeboda, R., Chodorowski, J., Turski, M., & Hajnos, M. (2018). Pore size distribution and stability of ortstein and overlying horizons in podzolic soils under forest. *Geoderma*, *310*, 138–142.

Meyer, N., Bornemann, L., Welp, G., Schiedung, H., Herbst, M., & Amelung, W. (2017). Carbon saturation drives spatial patterns of soil organic matter losses under long-term bare fallow. *Geoderma*, *306*, 89–98.

Mosaddeghi, M. R., Koolen, A. J., Hajabbasi, M. A., Hemmat, A., & Keller, T. (2007). Suitability of pre-compression stress as the real critical stress of unsaturated agricultural soils. *Biosystems Engineering*, *98*(1), 90–101.

Nimmo, J. R., & Perkins, K. S. (2002). Aggregate stability and size distribution. In J. H. Dane & G. C. Topp (Eds.), *Methods of soil analysis: Part 4, Physical methods* (Vol. 4, pp. 317–328). SSSA.

Otsu, N. (1979). A threshold selection method from gray-level histograms. *IEEE Transactions on Systems, Man, and Cybernetics*, *9*(1), 62–66.

R Core Team. (2018). *R: A language and environment for statistical computing*. R Foundation for Statistical Computing. https://www.R-project.org/

Reichert, J. M., Suzuki, L. E. A. S., Reinert, D. J., Horn, R., & Håkansson, I. (2009). Reference bulk density and critical degree-of-compactness for no-till crop production in subtropical highly weathered soils. *Soil and Tillage Research*, *102*(2), 242–254.

Rogowski, A. S. (1964). *Strength of soil aggregates* (2716) [Doctoral dissertation, Iowa State University]. Digital Repository. https://doi.org/10.31274/rtd-180813-17461

Rogowski, A. S., Moldenhauer, W. C., & Kirkham, D. (1968). Rupture parameters of soil aggregates. *Soil Science Society of America Journal*, *32*(5), 720–724.

Roldán, A., Caravaca, F., Hernández, M. T., Garcıa, C., Sánchez-Brito, C., Velásquez, M., & Tiscareno, M. (2003). No-tillage, crop residue additions, and legume cover cropping effects on soil quality characteristics under maize in Patzcuaro watershed (Mexico). *Soil and Tillage Research*, *72*(1), 65–73.

Safar, F., & Whalen, J. K. (2023). Mechanical stability of newly-formed soil macroaggregates influenced by calcium concentration and the calcium counter-anion. *Geoderma*, *430*, 116333. https://doi.org/10.1016/j.geoderma.2023.116333

Schindelin, J., Arganda-Carreras, I., Frise, E., Kaynig, V., Longair, M., Pietzsch, T., Preibisch, S., Rueden, C., Saalfeld, S., Schmid, B., Tinevez, J.-Y., White, D. J., Hartenstein, V., Eliceiri, K., Tomancak, P., & Cardona, A. (2012). Fiji: An open-source platform for biological-image analysis. *Nature Methods*, *9*(7), 676–682.

Schweizer, S. A., Aehnelt, M., Bucka, F., Totsche, K. U., & Kögel-Knabner, I. (2024). Impact of bare fallow management on soil carbon storage and aggregates across a rock gradient. *Journal of Plant Nutrition and Soil Science*, *187*, 118–129. https://doi.org/10.1002/jpln.202300156

Schweizer, S. A., Bucka, F. B., Graf-Rosenfellner, M., & Kögel-Knabner, I. (2019). Soil microaggregate size composition and organic matter distribution as affected by clay content. *Geoderma*, *355*, 113901. https://doi.org/10.1016/j.geoderma.2019.113901

Siebers, N., Voggenreiter, E., Joshi, P., Rethemeyer, J., & Wang, L. (2024). Synergistic relationships between the age of soil organic matter, Fe speciation, and aggregate stability in an arable Luvisol. *Journal of Plant Nutrition and Soil Science*, *187*, 77–88. https://doi.org/10.1002/jpln.202300020

Six, J. A. E. T., Elliott, E. T., & Paustian, K. (2000). Soil macroaggregate turnover and microaggregate formation: A mechanism for C sequestration under no-tillage agriculture. *Soil Biology and Biochemistry*, *32*(14), 2099–2103.

Tisdall, J. M., & Oades, J. M. (1982). Organic matter and water-stable aggregates in soils. *Journal of Soil Science*, *33*(2), 141–163.

Totsche, K. U., Amelung, W., Gerzabek, M. H., Guggenberger, G., Klumpp, E., Knief, C., Lehndorff, E., Mikutta, R., Peth, S., Prechtel, A., Ray, N., & Kögel-Knabner, I. (2018). Microaggregates in soils. *Journal of Plant Nutrition and Soil Science*, *181*(1), 104–136.

Uteau, D., Pagenkemper, S. K., Peth, S., & Horn, R. (2013). Aggregate and soil clod volume measurement: A method comparison. *Soil Science Society of America Journal*, *77*(1), 60–63.

Vogel, H. J. (1997). Morphological determination of pore connectivity as a function of pore size using serial sections. *European Journal of Soil Science*, *48*(3), 365–377.

Wang, P., & Arson, C. (2016). Discrete element modeling of shielding and size effects during single particle crushing. *Computers and Geotechnics*, *78*, 227–236.

Wuddivira, M. N., & Camps-Roach, G. (2007). Effects of organic matter and calcium on soil structural stability. *European Journal of Soil Science*, *58*(3), 722–727.

Zaher, H., & Caron, J. (2008). Aggregate slaking during rapid wetting: Hydrophobicity and pore occlusion. *Canadian Journal of Soil Science*, *88*(1), 85–97.

SUPPORTING INFORMATION

Additional supporting information can be found online in the Supporting Information section at the end of this article.

How to cite this article: Roosch, S., Felde, V. J. M. N. L., Uteau, D., & Peth, S. (2024). Exploring the mechanisms of diverging mechanical and water stability in macro- and microaggregates. *Journal of Plant Nutrition and Soil Science*, *187*, 104–117. https://doi.org/10.1002/jpln.202300245